JOINT CENTER FOR SATELLITE ASSIMILATION

NO.70, SUMMER 2021

JCSDA Quarterly

NOAA | NASA | US NAVY | US AIR FORCE

https://doi.org/10.25923/matc-am30

IN THIS ISSUE

JOINT CENTER FOR SATELLITE DATA ASSIMILATION

5830 University Research Court
College Park, Maryland 20740

3300 Mitchell Lane
Boulder, Colorado 80301

www.jcsda.org

NEWS IN THIS QUARTER

Static Background Error Covariance for the Model for Prediction Across Scales (MPAS) in Joint Effort for Data Assimilation Integration (JEDI)

Byoung-Joo Jung[1], Chris Snyder[1], Zhiquan Liu[1], and Benjamin Ménétrier[2,3]

[1] National Center for Atmospheric Research, Boulder CO , [2] IRIT, Toulouse, France, and [3] JCSDA, Boulder CO

Background

Under the Prediction and Data Assimilation for Cloud (PANDA-C) project, which is funded by the US Air Force and aimed at cloud analysis and forecasting, a variational data assimilation (DA) system is being developed for Model for Prediction across Scales (MPAS) model, within the Joint Effort for Data Assimilation Integration (JEDI) framework. This article summarizes the development of a multivariate static background error covariance (B) for MPAS within JEDI. For all the diagnostics and experiments, a 120 km quasi-uniform MPAS mesh (of 40,962 horizontal cells) is configured with 55 vertical levels with 30 km model top.

Multivariate background error covariance design

The basic design of the MPAS multivariate background error covariance follows that of the Weather Research and Forecasting (WRF) model DA (WRFDA; Barker et al. 2012) system and the Gridpoint Statistical Interpolation (GSI; Wu et al. 2002) system. The multivariate properties are implemented as a set of linear variable changes to a block-diagonal covariance matrix as: $B=K_1K_2\Sigma C\Sigma^T K_2^T K_1^T$. The linear variable changes K_1 and K_2 can be expressed in the following matrix forms:

$$K_1: \begin{bmatrix} \delta u \\ \delta v \\ \delta T \\ \delta sh \\ \delta p_s \end{bmatrix} = \begin{bmatrix} -\partial_y & -\partial_x & 0 & 0 & 0 \\ \partial_x & -\partial_y & 0 & 0 & 0 \\ 0 & 0 & I & 0 & 0 \\ 0 & 0 & 0 & I & 0 \\ 0 & 0 & 0 & 0 & I \end{bmatrix} \begin{bmatrix} \delta\psi \\ \delta\chi \\ \delta T \\ \delta sh \\ \delta p_s \end{bmatrix} \qquad K_2: \begin{bmatrix} \delta\psi \\ \delta\chi \\ \delta T \\ \delta sh \\ \delta p_s \end{bmatrix} = \begin{bmatrix} I & 0 & 0 & 0 & 0 \\ L & I & 0 & 0 & 0 \\ M & 0 & I & 0 & 0 \\ 0 & 0 & 0 & I & 0 \\ N & 0 & 0 & 0 & I \end{bmatrix} \begin{bmatrix} \delta\psi \\ \delta\chi_u \\ \delta T_u \\ \delta sh \\ \delta p_{s,u} \end{bmatrix}$$

Here, K_1 computes increments for zonal wind (u) and meridional wind (v) from spatial derivatives of stream function (ψ) and velocity potential (χ). K_1 and the corresponding adjoint operator, K_1^T are the model-dependent JEDI component that operates on the MPAS native mesh.

K_2 is a variable change to compute the balanced contributions from ψ to χ, temperature (T), and surface pressure (p_s) based on linear regression, and adds those contributions to the unbalanced variables chi_u, T_u and p_s,u, which are assumed uncorrelated. The use of vertical regression to define the balanced contributions follows Derber and Bouttier (1999). As in Derber and Bouttier (1999), we choose to use ψ on the full set of vertical levels as predictors for T and p_s on a given level, which makes *M* and *N* as full matrices. We retain ψ only on the same level as a predictor for χ, which makes *L* as a diagonal matrix. Note that the specific humidity (sh) does not have a multivariate correlation with other variables.

Lastly, $\Sigma C \Sigma^T$ is the block-diagonal covariance matrix for increments of stream function ψ, specific humidity (Q), and the unbalanced contributions to χ, T, and p_s. It is constructed from Σ, a diagonal matrix with elements of standard deviation for each unbalanced variable, and C, a block-diagonal correlation matrix whose blocks give the univariate spatial (horizontal and vertical) correlation for each variable.

The operations K_2, K_2^T, Σ, Σ^T, and C use the Background error on Unstructured Mesh Package (BUMP) in the System-Agnostic Background-Error Representation (SABER) repository, which is a generic component within JEDI, through the MPAS model interfaces.

Diagnosed B statistics

The background error statistics are diagnosed from 366 samples of the Global Forecast System (GFS) 48-h and 24-h forecast differences, spanning the months of March, April, and May 2018. Because the inverse operation of K1 on the native mesh is not available, a spherical harmonics-based NCAR Command Language (NCL) function is used on an intermediate lat/lon grid.

For regression coefficients, the auto-covariance and cross-covariance statistics were aggregated within +/- 10 degrees latitude bands to reflect the latitude-dependent balance characteristics. Also, a pseudo-inverse with 20 dominant modes (among total 55 modes) was used for the inverse of the auto-covariance matrix. Figure A shows the balanced part of T, χ, and p_s, for a given ψ field near 34 degrees North.

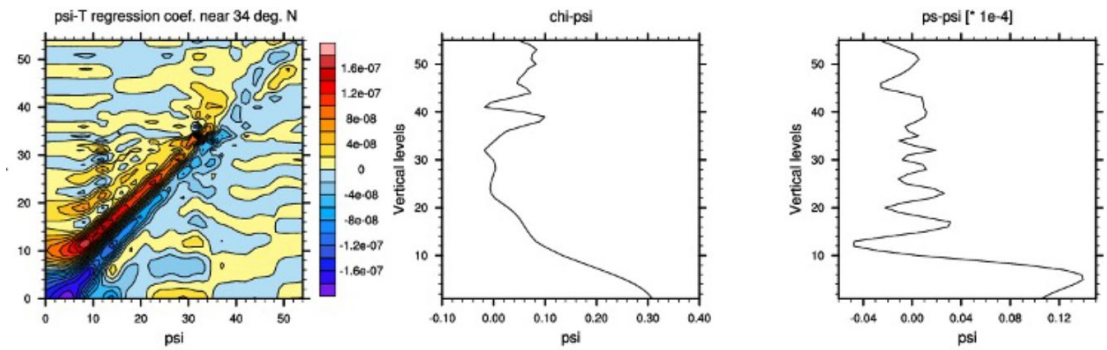

Figure A: The regression coefficients between ψ and T, ψ and χ, and ψ and p_s near 34 degrees North latitude.

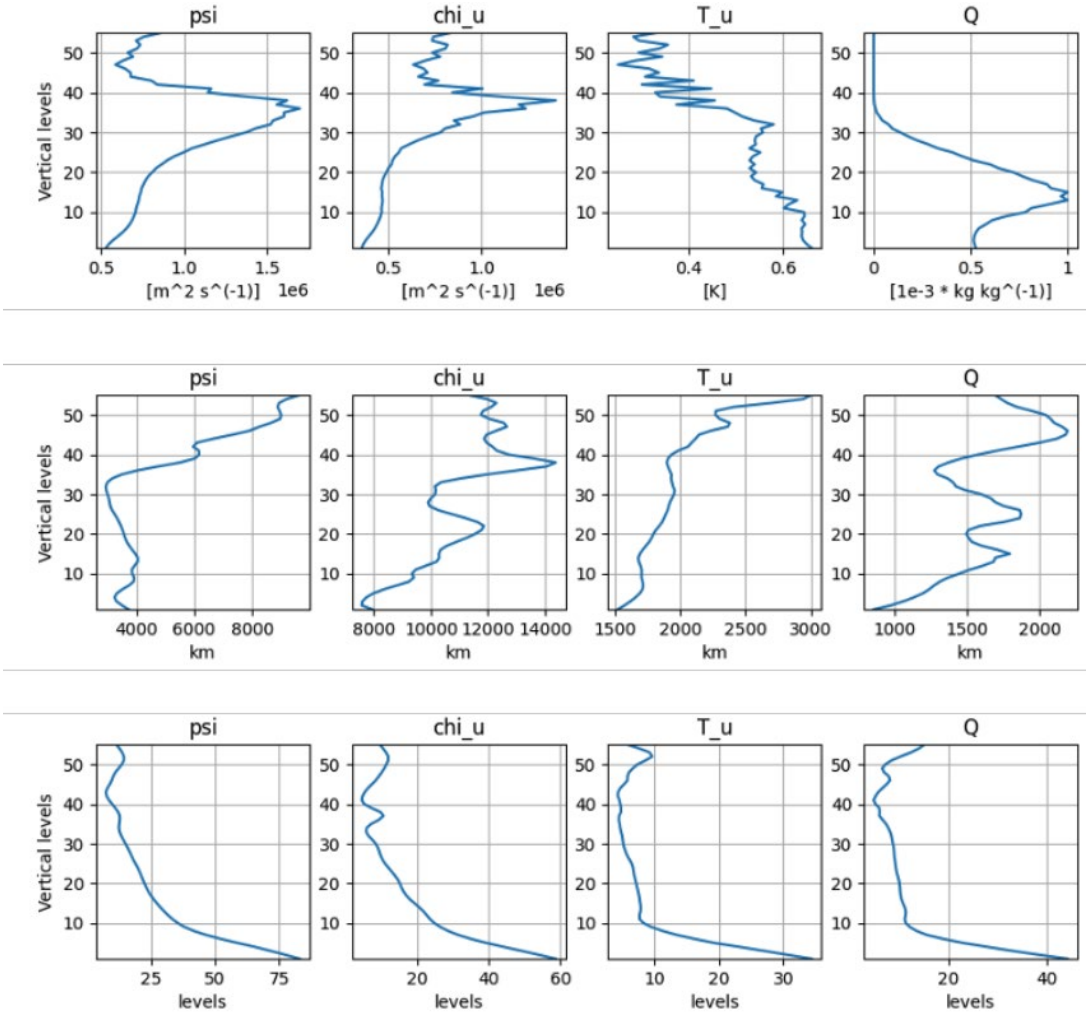

Figure B: Vertical profiles of domain-averaged (top) error standard deviations, (middle) horizontal length scales, and (bottom) vertical length scales for ψ, χ_u, T_u, and sh.

Figure B shows the vertical profiles of domain-averaged background error statistics for ψ, χ_u, T_u, and sh. The error standard deviation is diagnosed from BUMP VARiance (VAR) procedure and the horizontal and vertical length scales are diagnosed from BUMP Hybrid DIAGnostics (HDIAG) procedure. Note that the vertical coordinate for vertical length scale is in units of levels. The horizontal and vertical length scales for all the variables, but especially χ, are substantially larger than reported in other studies (e.g. Wu et al. 2002).

Single observation test

To explore the structure of multivariate B, a single zonal wind observation with 1 m s^{-1} innovation and 1 m s^{-1} observational error is placed at (102.95W, 26.57N) on the 10th model level, exactly on the model mesh. The resulting analysis increment fields are then proportional to the corresponding column of the B matrix, for a given observation. For comparison, we also present results from a univariate covariance matrix (of u, v, T, q, p_s, with variances and length scales estimated as for B and from a localized, ensemble-based covariance matrix. For the ensemble covariance, 20 members from The Global Ensemble Forecast System (GEFS) are used with the fixed localization scales (2000 km for horizontal and 5 levels for vertical radius). Figures C-F show the analysis increments for u, v, and T for the three covariance matrices on three vertical levels (6, 10, and 14th).

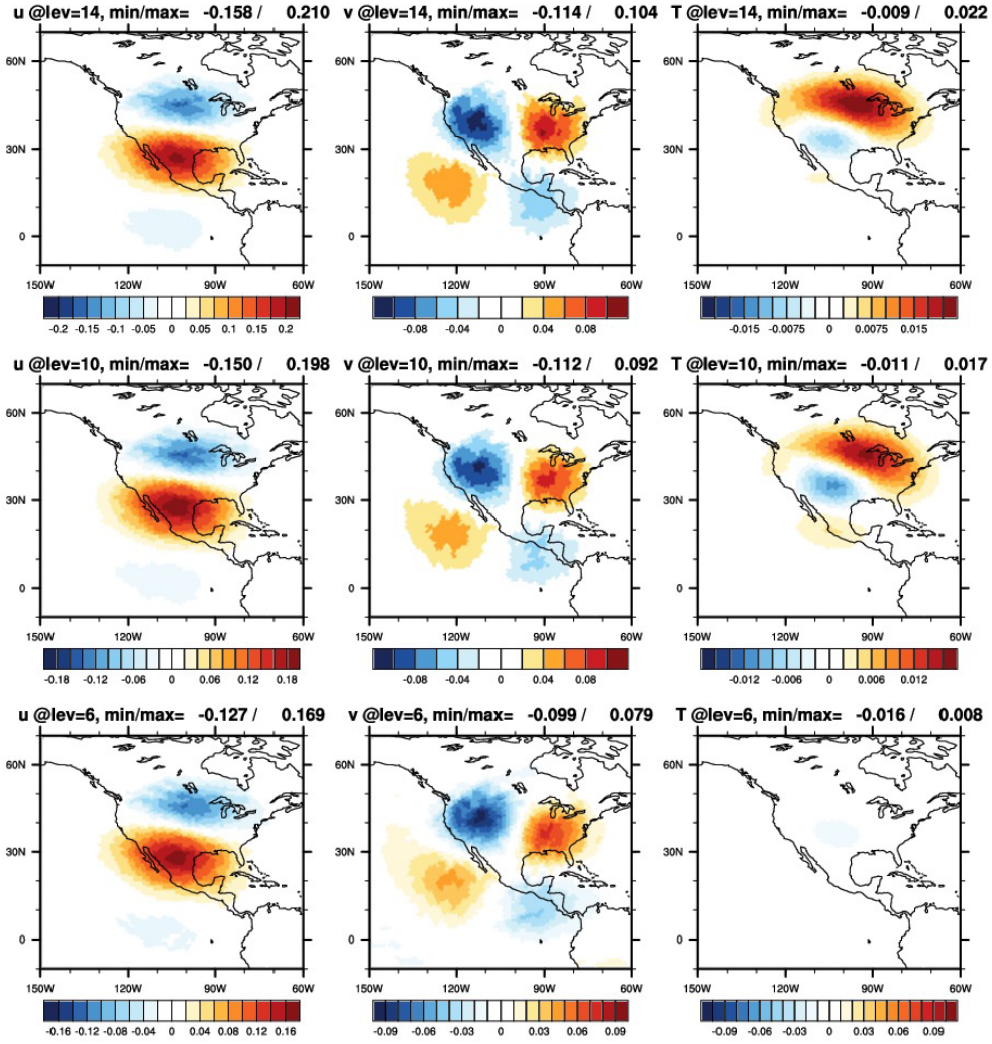

Figure C: Analysis increments for (left) u [m s^{-1}], (center) v [m s^{-1}], and (right) T [K] on the (top) 14th, (middle) 10th, and (bottom) 6th model vertical levels from raw multivariate B statistics.

The analysis increments from multivariate B reflect geostrophic balance in general: cyclonic (anti-cyclonic) circulation to the north (south) of the observation location and a warm temperature increment above the cyclonic circulation (Figure C). The analysis increment from univariate B has localized, isotropic structure without any increments in the unobserved variables (Figure D), while the analysis increment from ensemble B has the cross-variable covariances implicit in the ensemble of forecasts. Comparing the three analysis increments, the horizontal scales of increments from multivariate B are much larger than those from univariate B (Figure D) or ensemble B (Figure E). Also, the analysis fits the observation much less closely in the multivariate B test: the magnitudes of maximum U increment on the 10th model level (where the observation is placed) are 0.198, 0.659, and 0.497 m s^{-1} for multivariate, univariate, and ensemble covariances.

The length-scale diagnostics (HDIAG) in BUMP seek to fit the actual isotropic correlations to the fifth-order piecewise function of Gaspari and Cohn (1999), which resembles the Gaussian function. This function, however, differs from the actual correlations for stream function and velocity potential, which decay much more rapidly than a Gaussian at small

separations. To deal with this issue, the diagnosed multivariate B statistics are tuned: reducing the horizontal length scales for stream function and velocity potential as half of diagnosed values. This tuning procedure makes the horizontal scales of increments smaller (Figure F), and also produces a larger maximum U increment (from untuned 0.198 to tuned 0.504 at the model level 10), indicating a better fit-to-obs.

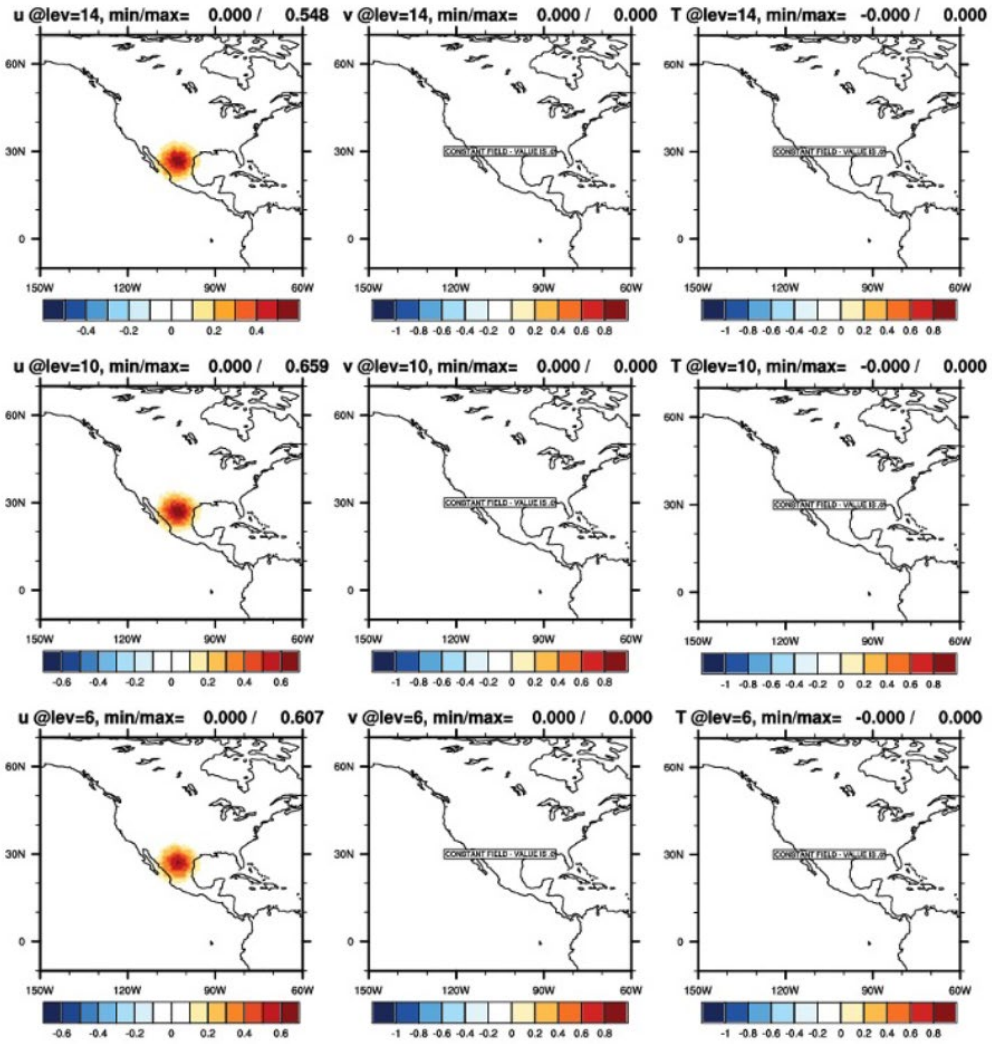

Figure D: Same as Figure C, except from univariate B statistics.

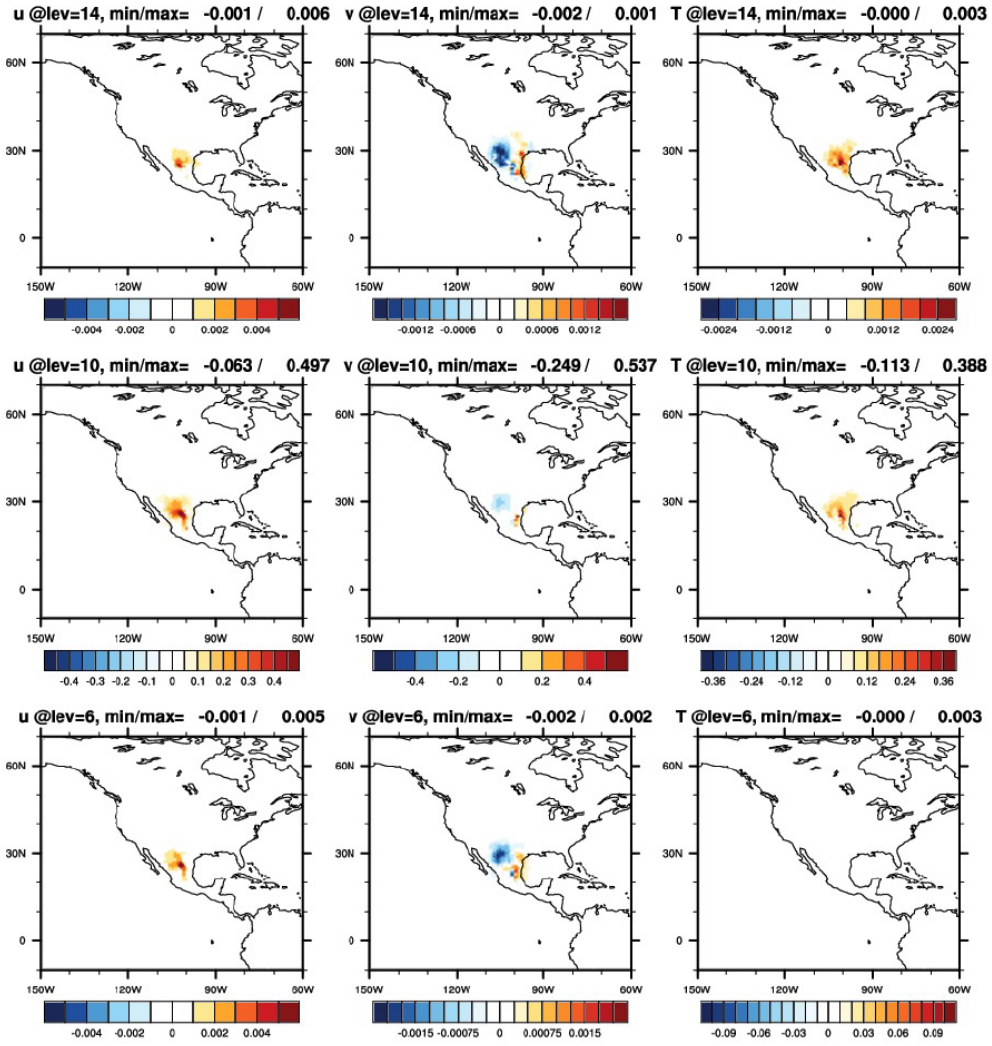

Figure E: Same as Figure C, except from ensemble B statistics.

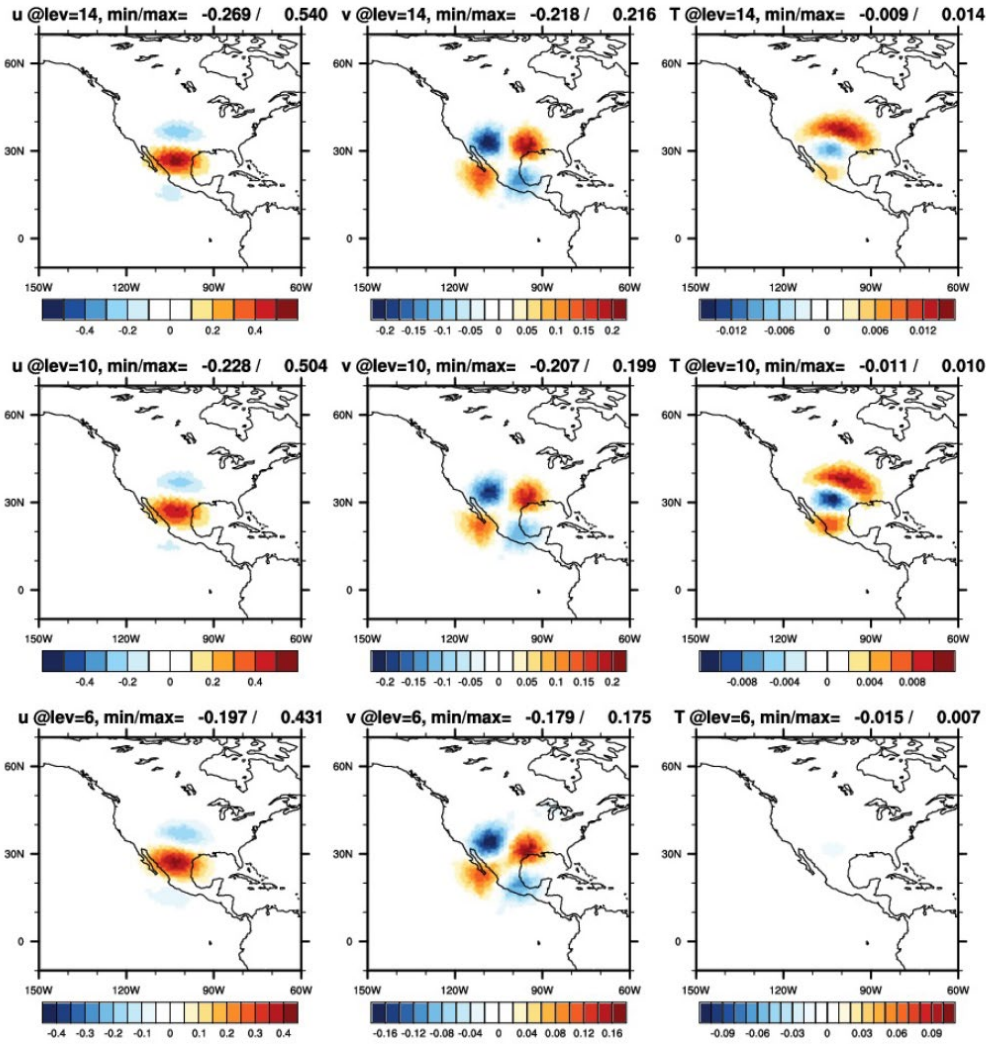

Figure F: Same as Figure C, except from multivariate B statistics with tuning.

Month-long cycling experiment

Month-long 3DVar cycling experiments using various static covariance matrices and assimilating the conventional observations and clear-sky AMSU-A radiances were performed at 120 km resolution starting from April 15 2018. Figure G shows the time-series of 6-hour forecast RMS error with respect to GFS analysis for surface pressure fields. In the northern extratropical (NXTro) region, multivariate B with tuning gives the smallest error. In the tropical (Tro) region, multivariate B with and without tuning give a similar error, but univariate B gives the largest error. In the southern extratropical (SXTro) region, the multivariate B with tuning gives a similar or smaller error, except for the latter 10 days.

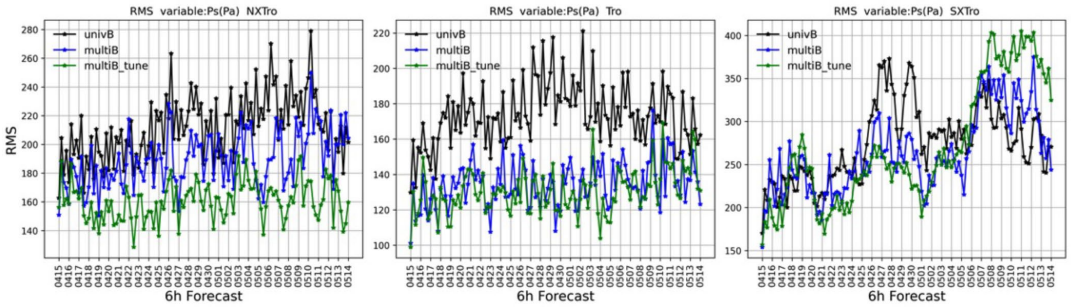

Figure G: Time-series of 6-hour forecast RMS error with respect to GFS analysis for surface pressure fields in (left) NXTro (30°N - 90°N), (center) Tro (30°S - 30°N), and (right) SXTro (30°S - 90°S) regions. UnivB: 3DVAR experiment with univariate B; multiB: 3DVAR experiment with multivariate B; univB_tune: multivariate B 3DVAR experiment with length scale tuning.

The extended 10-day forecasts were performed at each 00 UTC and the anomaly correlation coefficient (ACC) for 500 hPa geopotential height fields were compared between three month-long cycling experiments (Figure H). Overall, the experiment with a multivariate B with tuning gives the largest ACC values over all lead times. These results confirm that a careful evaluation and tuning of diagnosed background error statistics might be needed for better performance.

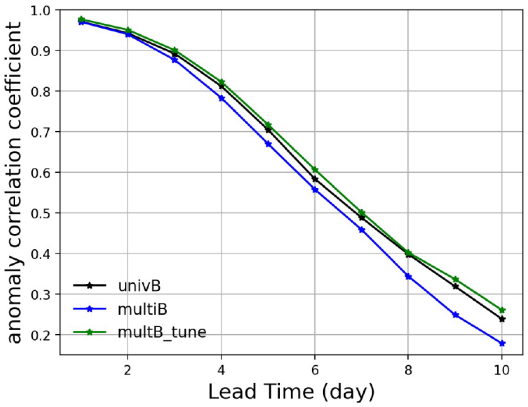

Figure H: Global anomaly correlation coefficient of 500 hPa geopotential height, 10-day forecast initialized at each 00 UTC.

The cycling experiments with hybrid covariance were also performed. In the experiment, the hybrid covariance was defined as a combination of a tuned static covariance and an ensemble covariance with equal weight, although this weight setting might not be an optimal choice. Again for ensemble covariance, 20 member GEFS ensembles were used with the fixed localization scales (2000 km for horizontal and 5 levels for vertical radius). Compared to pure static covariances, the hybrid covariances slightly improved the global 500 hPa height ACC scores up to 8 days lead time (Figure I). The improvement in the ACC scores over tropical regions is especially noticeable.

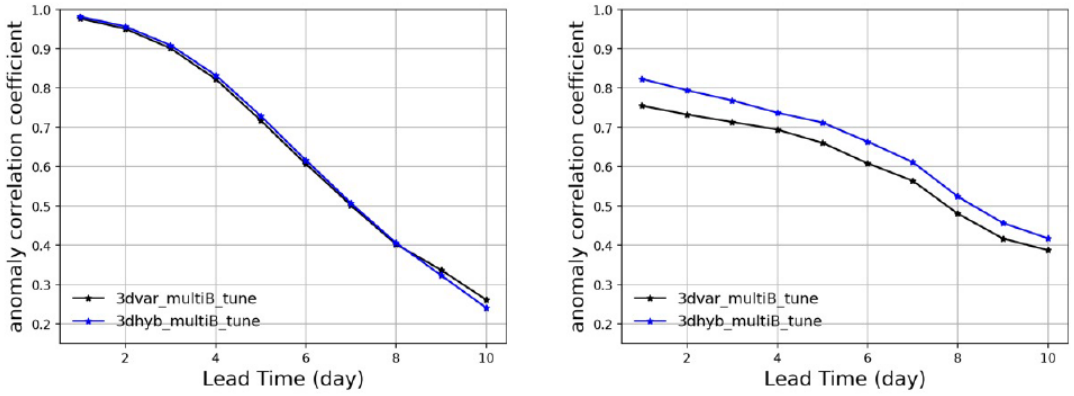

Figure I: Global (left) and tropical (right) anomaly correlation coefficient of 500 hPa geopotential height for multivariate 3dvar with tuning and the corresponding hybrid experiment, 10-day forecast initialized at each 00 UTC.

Summary

A multivariate static background error covariance for MPAS model is designed by using both model-specific and generic components within the JEDI framework. With 366 samples, the multivariate B statistics are diagnosed at MPAS 120 km quasi-uniform mesh. The structure of B was evaluated with a series of single observation tests and compared with pure ensemble covariance and univariate B. The tuning (halving the horizontal length scales for stream function and velocity potential) improved the horizontal scales of analysis increment and the fit-to-obs value. This tuning was confirmed to be beneficial in the month-long cycling experiment. We will continue further efforts to provide a better background error covariance, such as using a hybrid covariance, diagnosing the optimal hybrid weights, and diagnosing better/optimal correlation and localization length scales using MPAS model's own forecast.

Acknowledgements

This work was performed under the Prediction and Data Assimilation for Cloud (PANDA-C) project, funded by the US Air Force. This material is based upon work supported by the National Center for Atmospheric Research, which is a major facility sponsored by the National Science Foundation under Cooperative Agreement No. 1852977.

References

Barker, D., and Coauthors, 2012: The Weather Research and Forecasting Model's Community Variational/Ensemble Data Assimilation System: WRFDA. *Bull. Amer. Meteor. Soc.*, **93**, 831–843.

Derber, J., and F. Bouttier, 1999: A reformulation of the background error covariance in the ECMWF global data assimilation system. *Tellus A*, **51**, 195-221. doi:10.1034/j.1600-0870.1999.t01-2-00003.x

Gaspari, G., and S. E. Cohn, 1999: Construction of correlation functions in two and three dimensions. *Quart. J. Roy. Meteor. Soc.*, **125** , 723–757.

Wu, W.-S., , R. J. Purser, , and D. F. Parrish, 2002: Three-dimensional variational analysis with spatially inhomogeneous covariances. *Mon. Wea. Rev.*, **130** , 2905–2916.

Temperature-Dependent IR Sea Surface Emissivity (IRSSE) Model for the Community Radiative Transfer Model (CRTM)

Nicholas Nalli[1], James Jung[2], Ming Chen[3], Robert Knuteson[2], Jon Gero[2], and Ben Johnson[4]

[1] IMSG Inc. at NOAA/NESDIS/STA, [2] UW/CIMSS, [3] CICS-MD, [4] JCSDA

1 Background

For satellite thermal infrared (IR) remote sensing applications, the spectral *sea surface emissivity* must be specified with a high degree of absolute accuracy. A 1% uncertainty in emissivity can result in ≈0.2–0.6 K systematic error in hyperspectral longwave IR (LWIR) microwindow channel observations (e.g., Wu and Smith, 1996). Furthermore, in practice, the forward modeling problem also involves the necessity of correctly specifying the surface bidirectional reflectance distribution function (BRDF), because it is convolved with the direct emission. Because ocean surface waves have dimensions that are large with respect to IR wavelengths, and the surface is uniform within the field-of-view of passive IR sensors, the IR emissivity and reflectance problem may be treated from first principles within *physical models*.

2 IR Forward Modeling of Ocean Surfaces

Within satellite remote sensing forward and inverse modeling, physical models for IR sea-surface emissivity have been developed that have gained widespread acceptance (e.g., Masuda et al., 1988; Watts et al., 1996; Wu and Smith, 1997; Henderson et al., 2003; Masuda, 2006), but it is important to keep in mind that this was only after they were first empirically validated against field measure-ments. As a result, IR ocean emissivity has since almost been taken for granted by many as being a "solved problem." However, with the achievement of better-than 100 mK absolute accuracy in today's traceable, onboard-calibrated thermal IR sensors, additional problems in thermal IR models have been identified.

2.1 Emission-Only Models

Although models of IR sea-surface emission date back to the 1960s (e.g., Saunders, 1968), it was not until the late 1980s that IR emissivity models would begin to gain traction, beginning with Masuda et al. (1988), who published their calculations within a convenient print-version lookup table (LUT). However, the "Masuda model" was not widely used because it had not been validated against observations. It was not until the advent of the Marine Atmospheric Emitted Radiance Interferometer (MAERI) (Smith et al., 1996; Minnett et al., 2001) that application of emissivity models became possible in practice. In these conventional, emission-based models, *emissivity* is taken to be the ensemble-mean of one minus the Fresnel reflectance of visible surface wave facets.

2.2 Surface-Leaving Radiance Models

The problem with the approach of using these conventional emission-based emissivity models lies in the typical application to fast-model forward calculations (i.e., "*calc*") using either specular or Lambertian approximations for calculating the surface-leaving radiance (SLR). The specular approximation is the far more common approximation for water-surfaces, which are by definition *quasi-specular*, and is used by the the Community Radiative Transfer Model (CRTM) (van Delst et al., 2009). The Lambertian approximation may be conveniently applied to all surface types (land and sea), and is currently used by the Stand Alone Radiative Transfer Algorithm (SARTA) (Strow et al., 2003; DeSouza-Machado et al., 2020), but may in fact be oversimplified for quasi-specular water surfaces.

Within operational fast-model frameworks, these approximations are necessary because the actual RTE for water surfaces involves a hemispheric double-integral over varying 2-D wave slopes, each of these involving a downwelling radiance calculation at an arbitrary zenith angle. But because of the non-linear increases of both downwelling atmospheric radiance and the Fresnel reflection co-efficient as a function of θ , over the normal range of satellite view angles it is generally the case that the specular approximation will result in an systematic underestimation of SLR. This systematic underestimation has been consistently observed in MAERI spectra at larger zenith angles ($\theta_0 \geq 40^\circ$), where it is found to be on the order of 0.1–0.4 K in magnitude. This will also be the case for the Lambertian approximation for angles not equal to the assumed diffusivity angle, in addition to the likelihood of other biases at smaller angles.

A handful of previous investigators have sought to obtain practical solutions to the quasi-specular forward radiance problem (e.g., Watts et al., 1996; Nalli et al., 2001), but these ultimately were still not satisfactory for existing operational algorithms and models. Thus, an alternative approach was desirable. In 2005–2006, the Joint Center for Satellite Data Assimilation (JCSDA) and NOAA/STAR thus supported in-house research to find a workable solution for application to the CRTM. This JSCDA-funded research resulted in the CRTM IRSSE model (Nalli et al., 2008b,a; van Delst et al., 2009). Notably, the IRSSE model uses the principle of *effective emissivity* to account for the quasi-specular BRDF in a practical manner for operational fast-models.

2.3 Effective-Emissivity for Fast-Models

Effective emissivity is the guiding principle behind cavity blackbodies (e.g., Prokhorov, 2012; Schalles and Blumröder, 2012) commonly used for calibration of IR sensors. While the cavity's surface is not inherently black, its macroscale roughness creates multiple emissions and reflections off individual finite surface elements that effectively enhances the emissivity of the macroscale cavity. Thus, while the inherent "optical" emissivity of the cavity's surface elements are non-black, the macroscale cavity nevertheless *appears* black to the sensor given that it does not discriminate between directly emitted or multiply reflected contributions to the radiance. The same principle holds for any natural rough surface, including the sea surface.

The theoretical basis for the effective emissivity model may be derived from the conical-directional reflectance for non-isotropic incident radiation (Nicodemus, 1965; Nicodemus

et al., 1977). The *effective emissivity* is derived as a function of an effective emission angle, Θ_e, which is obtained iteratively via least-squares spectral minimizations over finite IR spectral intervals $\Delta\nu$ based on the exact quasi-specular RTE. In this manner, the effective angle is determined by bringing the simplified model into agreement with the full quasi-specular model as a function of view angle, wind speed and SST, (i.e., θ_0, $\bar{u}$, T_s). From Θ_e, the entire IR emissivity spectrum may then be determined and expressed as lookup tables for various given mean-square slope PDF models (e.g., Cox and Munk, 1954; Ebuchi and Kizu, 2002) and complex refractive indices (N_ν). This then allows a simplified quasi-specular RTE for the SLR that conveniently retains the familiar 2-term, 3-parameter form. The effective emissivity is thus defined in a manner practical for field measurements and fast forward modeling, keeping in mind that it is the observable radiance, $R_{\nu s}$, as opposed to a theoretical emissivity, ε_ν , that is the ultimate goal in forward modeling for remote sensing applications.

3 Accounting for Emissivity Temperature Dependence

While it has been known that there was a spectral dependence on surface temperature (e.g., Newman et al., 2005; Nalli et al., 2008a), it was not until recent findings of Liu et al. (2019) that a significant systematic bias (on the order of 0.5 K) was revealed to occur on a global scale in cold waters (i.e., the North Atlantic and Southern Oceans). The temperature dependence arises from changes to the refractive index of water associated with corresponding changes in density. This has brought attention back to this issue, which has since led to additional JCSDA (FY19–FY20) and JPSS support for model upgrades to address this problem.

3.1 Observed Global Biases

To investigate the global impact further, we performed a global analysis of spectral double-differences of obs − calc using 2-weeks NOAA-20 CrIS data using to isolate the emissivity signal (Fig. 1) while minimizing signals due to uncertainties in the atmospheric column (e.g., model bias, cloud contamination, H_2O errors, etc.). Using laboratory derived temperature-dependent (*T*-dep) reflectance ratios reported in Pinkley et al. (1977), we were able to isolate spectral channels with and without sensitivity to surface temperature, namely 939.25 cm^{-1} and 962.5 cm^{-1}. The obs − calc double-differences were computed as

$$\Delta[\Delta T_B(\nu)] = [T_B(\nu) - T_B(\nu_0)] - [\widehat{T}_B(\nu) - \widehat{T}_B(\nu_0)],$$

where $\widehat{T}_B$ denote estimates (i.e., calculations or background), ν_0 is a spectral channel known to exhibit negligible emissivity sensitivity to temperature, and ν are channels known to have varying degrees of sensitivity. The lefthand plots of Fig. 1 show a significant, near-linear trend in global observation minus background (obs − calc, also denoted $O - B$) over the range of ocean surface temperatures (271–305 K), with systematic biases varying on the order of 0.5 K. For comparison, the righthand plots show simulated double-differences for the same channel combinations assuming a global mean surface temperature based on Fresnel calculations using *T*-dep optical constants derived from the Pinkley reflectance data (Nalli et al., manuscript in prep; see below). Comparable linear trends are observed in the simulated double-differences, corroborating the hypothesis that the trends seen in Fig. 1 are in fact due to emissivity temperature dependence. Significant surface-temperature dependence = 0.5 K is clearly visible. Such systematic uncertainty magnitudes are of first order significance within the context of the total forward model uncertainty.

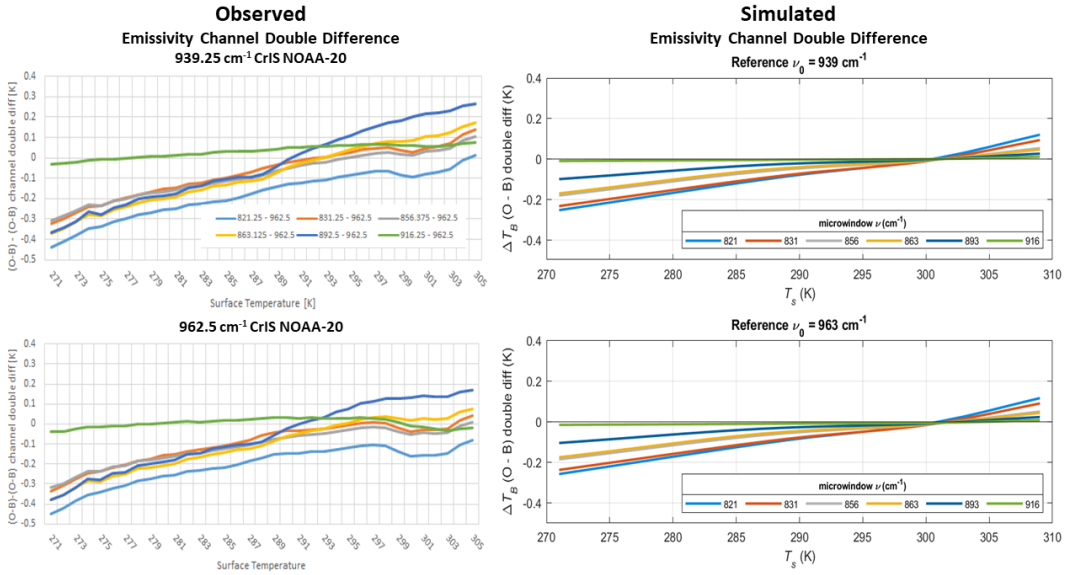

Figure 1: Global double-differences showing temperature dependence on surface emissivity using channels chosen to isolate the emissivity temperature-dependence signal based on Pinkley et al.(1977): (left column) 2-weeks global NOAA-20 CrIS data (*O*) versus CRTM model background calculations (*B*) using the IRSSE model v1.2 without temperature dependence, and (right column) simulated global double-differences showing temperature dependence on surface emissivity using *T*-dep optical constants derived from the Pinkley et al. (1977) laboratory measured reflectance ratios.

3.2 Temperature-Dependent Model

Temperature dependence in IR sea-surface emissivity arises from the dependence of the IR complex refractive index, N_ν, on the water density. Thus, the model may be extended to include temperature dependence simply through the application of a suitable set of optical constants that include temperature dependence. To our knowledge, the only complete set of laboratory derived *T*-dep IR reflectance measurements of water at varying surface temps were obtained by Pinkley et al. (1977). However, they only published a small subset of their derived optical constants, severely truncated to only 3 significant digits. Later, Newman et al. (2005) published field-derived values for the long-wave window region of the IR spectrum, and most recently Rowe et al. (2020) derived values for supercooled water temperatures.

When the IRSSE upgrade was first attempted in 2018–2019, the Rowe data were not yet available, and a decision was made to utilize the Pinkley data due to the fact that they included the full IR spectrum. However, as mentioned above, their published Table I did not include the complete dataset, and the remaining portions suffered precision losses due to truncation. The lead author (Nalli) thus attempted to contact the surviving members of Pinkley et al. (1977) (L. W. Pinkley, P. P. Sethna, or D. Williams), but subsequently found that both Pinkley and Williams have unfortunately been deceased since 2004, with the whereabouts and status of Sethna remaining unknown.

In lieu of this, an *ad hoc* approach was attempted to "rescue" the data based on digitization of of two figures from their paper (Figures 3 and 4, *op. cit.*). Ultimately, images from the original hardbound print copies were needed because the PDF reprint was illegible for digitation purposes; at our request the NOAA library provided us with high-resolution scans which are reproduced here in Fig. 2. However, ultimately this effort was still considered to be sub-optimal given that these figures were not well-suited for digitization, with different temperature values overlapping each other at this scale, together with the image scans themselves being distorted from the hardbound photocopy.

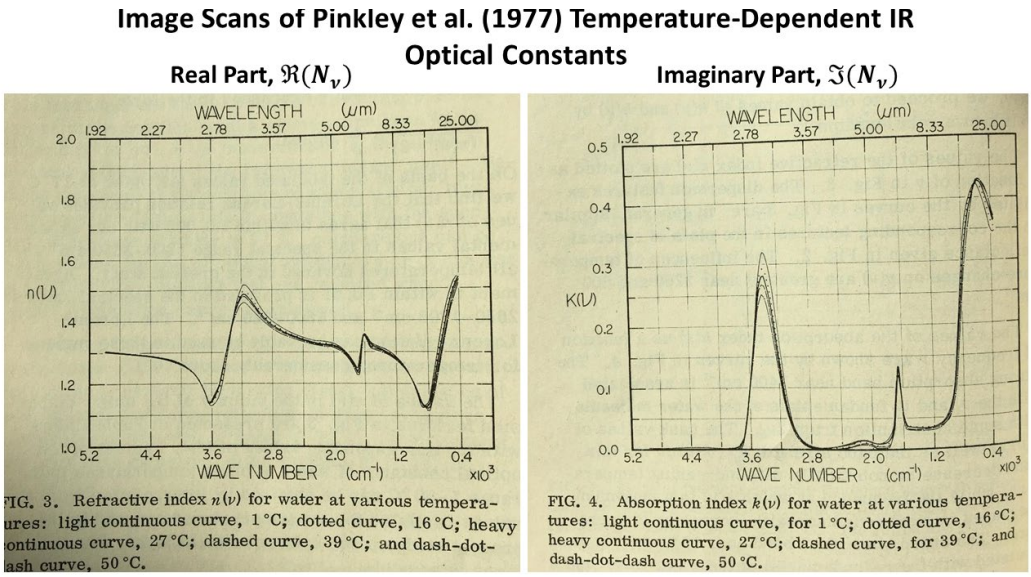

FIG. 3. Refractive index $n(\nu)$ for water at various temperatures: light continuous curve, 1 °C; dotted curve, 16 °C; heavy continuous curve, 27 °C; dashed curve, 39 °C; and dash-dot-dash curve, 50 °C.

FIG. 4. Absorption index $k(\nu)$ for water at various temperatures: light continuous curve, for 1 °C; dotted curve, 16 °C; heavy continuous curve, 27 °C; dashed curve, 39 °C; and dash-dot-dash curve, 50 °C.

Figure 2: Digital image scans of *T*-dep IR optical constants of water from the hard-bound copy of the Pinkley et al. (1977) paper (Figures 3 and 4, *op. cit.*) used for the initial *ad hoc* "data rescue" digitation; the real and imaginary parts of the complex refractive indices, N_v are shown on the left and right plots, respectively.

Based on the Pinkley data digitation, a preliminary upgrade to the IRSSE model (v2.0) was performed, and an infrastructure was developed for testing (discussed more below). Like the previous model, the new model output is encapsulated in the form of a convenient multidimensional LUT, albeit expanded to include a fourth dimension, namely the surface temperature. The emissivity is thus expressed as a function of wave number ν, zenith angle θ_0, surface wind speed $\bar{u}$, and surface temperature T_s. The initial results of from the preliminary model upgrade were encouraging.

Following this initial effort, the authors were made aware of the Rowe et al. (2020) data at the December 2020 International Space Science Institute (ISSI) Reference Quality Ocean Emissivity Model Team Meeting (English et al., 2020). Because of the suboptimal nature of the *ad hoc* Pinkley digitization, along with feedback from assimilation runs performed with NOAA/NCEP Global Data Assimilation System (GDAS) Gridpoint Statistical Interpolation (GSI) assimilation system (Kleist et al., 2009), another effort was made to assemble a *T*-dep dataset by merging the Rowe data with existing published datasets taken at room temperature (e.g., Pontier and Dechambenoy, 1966; Hale and Querry, 1973; Downing and Williams, 1975; Segelstein, 1981; Wieliczka et al., 1989; Bertie and Lan, 1996). The Rowe data contained one useful set of measurements for this purpose, namely values measured at 273 K; values for temperatures between 273 K and existing published datasets taken at room temperatures (which ranged from 298–303 K) would then be obtained via interpolation. This led to another upgrade to the IRSSE model (v2.1), with seperate LUT generated for each of the sets of merged optical constants and two different wave slope PDF models (i.e., Cox and Munk, 1954; Ebuchi and Kizu, 2002).

As mentioned above, a testing/validation infrastructure was set up to test the new versions of the model, which consists of both offline and CRTM-implementations. The offline LUT are first tested using synthetic global data (based on NOAA89 radiosonde profiles), ship-based MAERI data, and global AIRS/ECMWF collocations using the kCARTA model (DeSouza-Machado et al., 2020) in collaboration with Sergio DeSouza-Machado (UMBC). After going through these offline tests, the LUT are delivered to the CRTM Team for implementation within the CRTM Community Surface Emissivity Module (CSEM), which then allows testing within GSI assimilation runs.

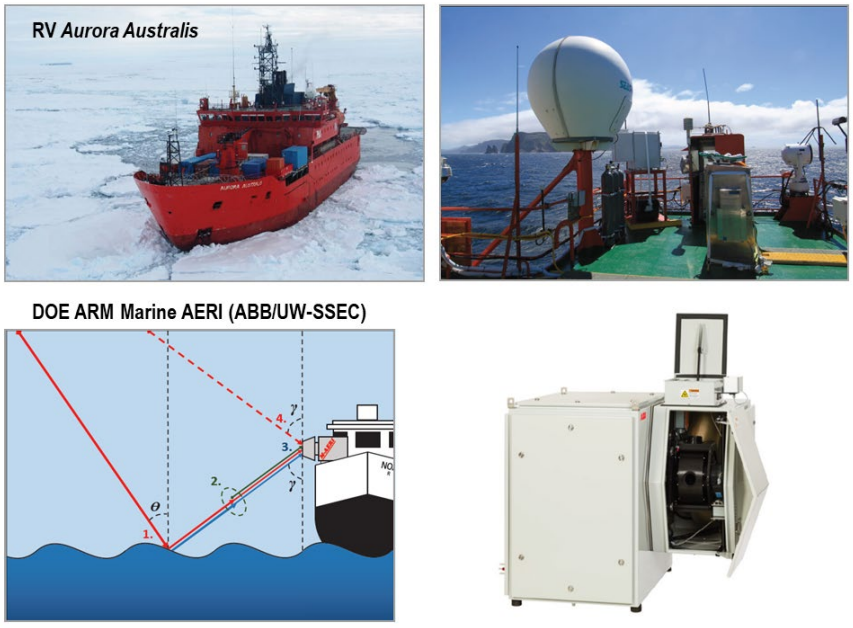

Figure 3: The ARM Mobile Facility-2 (AMF2) MAERI instrument deployed during the cold-water 2017 Measurements of Aerosols, Radiation, and Clouds over the Southern Ocean (MARCUS): (top left) the icebreaker RV *Aurora Australis*, (top right) view of MAERI on the deck, (bottom left) schematic of the MAERI observing configuration, and (bottom right) photo of the AMF2 MAERI showing the view port.

High-resolution, well-calibrated IR spectra were obtained from two field campaigns, namely the 2017 Measurements of Aerosols, Radiation, and Clouds over the Southern Ocean (MARCUS)(Gero et al., 2019) (Fig. 3), and the 1996 Combined Sensor Program (CSP) (Post et al., 1997) campaigns. MARCUS was conducted over the Southern Ocean in cold waters and CSP over the Tropical Western Pacific Warm Pool (warm waters).

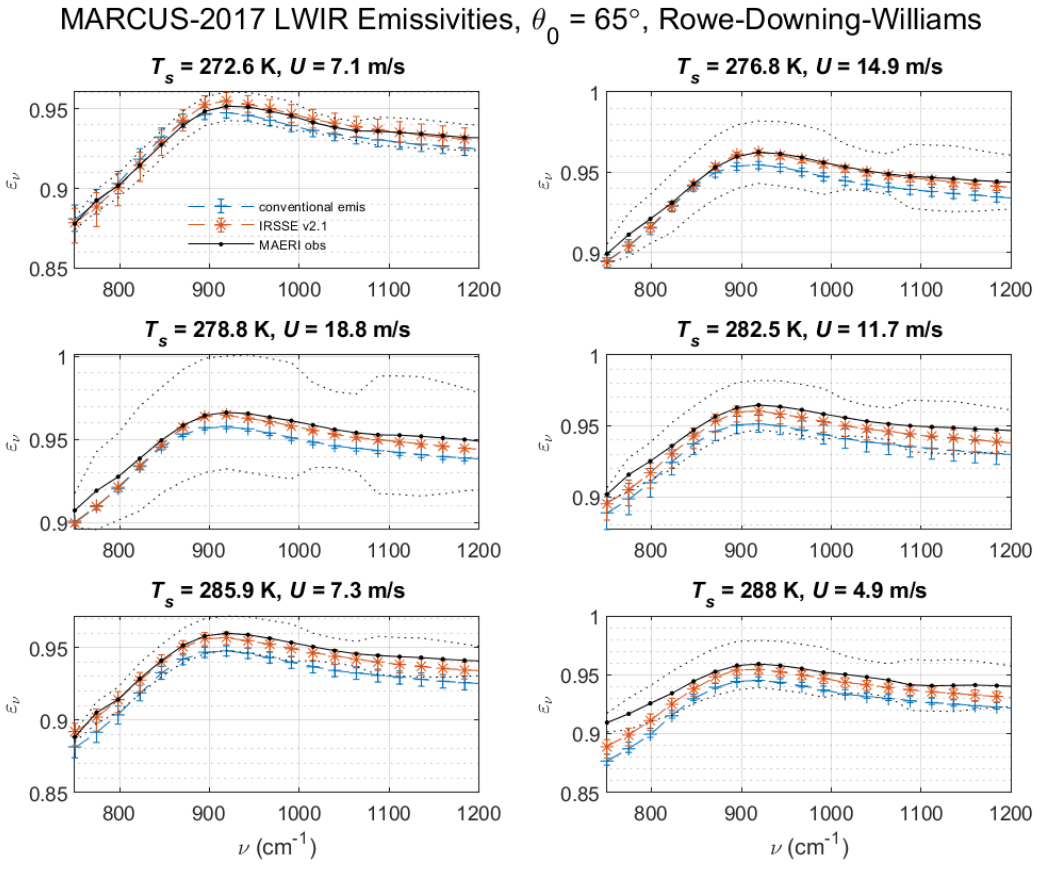

Figure 4: Longwave IR (LWIR) emissivity comparison between the IRSSE v2.1 (red), "conventional" emission-only (Masuda, 2006) (blue), and MAERI observations (black ±1σ uncertainty in the mean) obtained during the 2017 cold-water MARCUS campaign. The 6 plots are arranged in SST bins from cold to warmer waters; the mean SST and surface windspeeds are indicated in the titles. The model calculations here were based upon the Cox and Munk (1954) wave slope statistics.

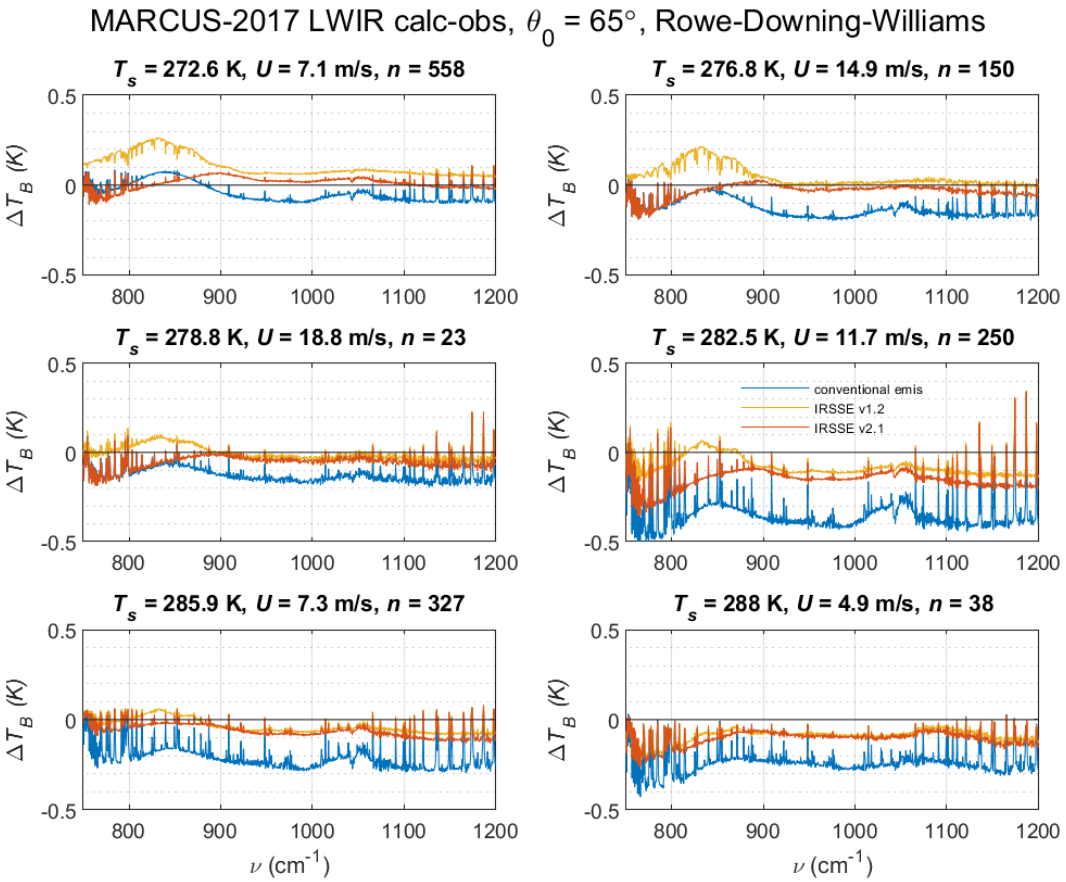

Figure 5: As Fig. 4, except showing calc − obs and including the results from the v1.2 IRSSE model, derived without temperature-dependence, for comparison (gold).

Figures 4 and 5 show comparisons of the IRSSE model upgrade (v2.1) based on merged optical constants, Rowe et al. (2020) with Downing and Williams (1975), versus the MAERI observations taken at $\theta_0 = 65°$ emission angle from the MARCUS campaign. Note that in our comparisons against MAERI observations, both the SLR and downwelling atmospheric radiance are directly observed, and T_S is retrieved as described in Smith et al. (1996) and Hanafin and Minnett (2005). Figure 4 shows the direct comparison between the MAERI-observed and modeled emissivities, ε_ν, in the longwave IR (LWIR) window region, 750–1200 cm^{-1} (≈ 8–13 μ m). These plots show the familiar spectral variation in water emissivity in the LWIR, but also show the underestimation of effective emissivity by conventional emission-only models (Masuda, 2006) at larger observing angles. However, we can get a better sense for the magnitude of the errors in Fig. 5, which shows the calc − obs results in equivalent brightness temperatures. Here one may see the magnitude in the systematic underestimation of conventional emission-only models to be on the order of 0.1–0.4 K. However, one may also see the introduction of T-dep errors below 900 cm^{-1} for the colder water cases (i.e., the top 4 plots). It should be noted that most narrowband satellite imagers designed for accurate retrieval of SSTs incorporate a "split-window" with at least one channel sensitive to this portion of the spectrum; for example, the spectral response of Channel 16 of the JPSS VIIRS instrument spans approximately 815–876 cm^{-1}.

4 Ongoing and Future Work

Based on feedback from GSI assimilation runs, there has remained some residual biases in the region of 880–920 cm^{-1} in both preliminary versions v2.0 and v2.1. Because of the

sub-optimal approaches for obtaining temperature-dependent IR optical constants of water described above, we have now pursued a rigorous data-rescue using the Pinkley et al. (1977) measured reflectances, along with Kramers-Kronig (KK) analysis (e.g., Stegmann and Yang, 2017) to derive temperature-dependent optical constants from existing datasets . Among other things, the electronic PDF reprint of their reflectance-ratio figure (Fig. 1, *op. cit.*) is legible and conducive to accurate digitization, which then allows for a direct derivation of *T*-dep optical constants (basically duplicating Pinkley's methodology) for each of the existing standard datasets.

Based on these data, a new set of v2.2 IRSSE LUT have been generated, tested, and delivered to the CRTM team, with GSI assimilation tests to follow, along with additional MAERI validation based on data from the 2015 CalWater/ACAPEX campaign (e.g., Gero et al., 2016). We also seek to facilitate implementation within other fast forward models, including SARTA, kCARTA, PCRTM, ISSI, among others. In the near-term we plan to publish the *T*-dep optical constants derived from the KK methodology as a journal note or letter (e.g., *Optics Letters or IEEE-GRSL*), noting that a new set of laboratory-measured IR optical constants of water could based upon this methodology, and may ultimately be desirable to minimize remaining residual temperature-dependent global biases in thermal IR surface window channels.

Acknowledgments

This work has been supported by the JSTAR Cal/Val Program (Lihang Zhou), JPSS PGRR (Mitch Goldberg), JCSDA (Kevin Garrett), and the STAR NUCAPS Soundings Team (K. Pryor, S. Kalluri, C. Tan, T. Zhou, M. Divakarla, et al.). We also acknowledge Stephen English, Stuart Newman and the ISSI Reference Ocean Surface Emissivity Model Team for their support, along with Patrick Stegmann (JCSDA) for sharing his expertise on using KK-analysis. kCARTA/SARTA improvements (S. DeSouza-Machado and L. Strow) are funded by the NASA AIRS Sounder Team. MAERI data are provided by UW/CIMSS and UM/RSMAS (Peter Minnett, G. Szczodrak, M. Izaguirre). The views, opinions and findings contained in this report are those of the authors and should not be construed as an official NOAA or U.S. Government position, policy or decision.

References

Bertie, J. E. and Z. Lan, 1996: Infrared intensities of liquids. xx. the intensity of the oh stretching band of liquid water revisited and the best current values of the optical constants of h_2o (l) at 25c between 15,000 and 1 cm^{-1}. *Appl. Spectrosc.*, **50**, 1047–1057.

Cox, C. and W. Munk, 1954: Measurements of the roughness of the sea surface from photographs of the sun's glitter. *J. Opt. Soc. Am.*, **44**, 838–850.

DeSouza-Machado, S., L. L. Strow, H. Motteler, and S. Hannon, 2020: kCARTA: a fast pseudo line-by-line radiative transfer algorithm with analytic Jacobians, fluxes, nonlocal thermodynamic equi-librium, and scattering for the infrared. *Atmos. Meas. Tech.*, **13 (1)**, 323–339, doi:10.5194/amt13-323-2020.

Downing, H. D. and D. Williams, 1975: Optical constants of water in the infrared. *J. Geophys. Res.*, **80 (12)**, 1656–1661.

Ebuchi, N. and S. Kizu, 2002: Probability distribution of surface wave slope derived using sun glitter images from geostationary meteorological satellite and surface vector winds from scatterometers. *J. Oceanography*, **58**, 477–486.

English, S., et al., 2020: Reference-quality emission and backscatter modeling for the ocean. *Bulletin of the American Meteorological Society*, **101 (10)**, E1593 – E1601, doi:10.1175/BAMS-D-20-0085.1.

Gero, P. J., R. O. Knuteson, N. R. Nalli, and J. Jung, 2019: Retrievals of sea surface emissivity and skin temperature from M-AERI Observations from the MARCUS cam-paign. *AGU Fall Meeting*, San Francisco, CA, USA, American Geophysical Union, https://agu.confex.com/agu/fm19/meetingapp.cgi/Paper/556881.

Gero, P. J., M. Westphall, R. O. Knuteson, W. L. Smith, and N. R. Nalli, 2016: Retrievals of sea sur-face emissivity and skin temperature from M-AERI Observations from the ACAPEX/CalWater2 campaign. *AGU Fall Meeting*, San Francisco, CA, USA, American Geophysical Union, https://agu.confex.com/agu/fm16/meetingapp.cgi/Paper/140168.

Hale, G. M. and M. R. Querry, 1973: Optical constants of water in the 200-nm to 200-μm wavelength region. *Appl. Opt.*, **12**, 555–563.

Hanafin, J. A. and P. J. Minnett, 2005: Measurements of the infrared emissivity of a wind-roughened sea surface. *Appl. Optics*, **44 (3)**, 398–411.

Henderson, B. G., J. Theiler, and P. Villeneuve, 2003: The polarized emissivity of a wind-roughened sea surface: A Monte Carlo model. *Rem. Sens. Environ.*, **88**, 453–467.

Kleist, D. T., D. F. Parrish, J. C. Derber, R. Treadon, W.-S. Wu, and S. Lord, 2009: Introduction of the GSI into the NCEP Global Data Assimilation System. *Weather and Forecasting*, **24 (6)**, 1691–1705, doi:10.1175/2009WAF2222201.1.

Liu, E. H., et al., 2019: EMC contributions to CRTM development and validation. *JCSDA Quarterly*, **63**, doi:10.25923/c23x-ac34.

Masuda, K., 2006: Infrared sea surface emissivity including multiple reflection effect for isotropic gaussian slope distribution model. *Remote Sens. Environ.*, **103**, 488–496.

Masuda, K., T. Takashima, and Y. Takayama, 1988: Emissivity of pure and sea waters for the model sea surface in the infrared window regions. *Remote Sens. Environ.*, **24**, 313–329.

Minnett, P. J., R. O. Knuteson, F. A. Best, B. J. Osborne, J. A. Hanafin, and O. B. Brown, 2001: The Marine-Atmospheric Emitted Radiance Interferometer (M-AERI): a high-accuracy, sea-going in-frared spectroradiometer. *J. Atmos. Oceanic Tech.*, **18**, 994–1013.

Nalli, N. R., P. J. Minnett, E. Maddy, W. W. McMillan, and M. D. Goldberg, 2008a: Emissivity and reflection model for calculating unpolarized isotropic water surface leaving radiance in the infrared. 2: Validation using Fourier transform spectrometers. *Appl. Optics*, **47 (25)**, 4649–4671.

Nalli, N. R., P. J. Minnett, and P. van Delst, 2008b: Emissivity and reflection model for

calculating unpolarized isotropic water surface leaving radiance in the infrared. 1: Theoretical development and calculations. *Appl. Optics*, **47 (21)**, 3701–3721.

Nalli, N. R., W. L. Smith, and B. Huang, 2001: Quasi-specular model for calculating the reflection of atmospheric emitted infrared radiation from a rough water surface. *Appl. Optics*, **40 (9)**, 1343–1353.

Newman, S. M., J. A. Smith, M. D. Glew, S. M. Rogers, and J. P. Taylor, 2005: Temperature and salinity dependence of sea surface emissivity in the thermal infrared. *Q. J. R. Meteorol. Soc.*, **131**, 2539–2557.

Nicodemus, F. E., 1965: Directional reflectance and emissivity of an opaque surface. *Appl. Optics*, **4 (7)**, 767–773.

Nicodemus, F. E., J. C. Richmond, J. J. Hsia, I. W. Ginsberg, and T. Limperis, 1977: Geometrical considerations and nomenclature for reflectance. Tech. Rep. NBS MN-160, National Bureau of Standards, U.S. Department of Commerce, Washington, D.C.

Pinkley, L. W., P. P. Sethna, and D. Williams, 1977: Optical properties of water in the infrared: Influence of temperature. *J. Opt. Soc. Am.*, **67 (4)**, 494–499.

Pontier, L. and C. Dechambenoy, 1966: Determination des constantes optiques de l'eau liquide entre 1 et 40 microns. application au calcul de son pouvoir reflecteur et de son emissivite. *Ann. Geophys.*, **22**, 633–641.

Post, M. J., et al., 1997: The Combined Sensor Program: An air–sea science mission in the central and western Pacific Ocean. *Bull. Am. Meteorol. Soc.*, **78 (12)**, 2797–2815.

Prokhorov, A., 2012: Effective emissivities of isothermal blackbody cavities calculated by the monte carlo method using the three-component bidirectional reflectance distribution function model. *Appl. Opt.*, **51 (13)**, 2322–2332.

Rowe, P. M., M. Fergoda, and S. Neshyba, 2020: Temperature-dependent optical properties of liquid water from 240 to 298 K. *J. Geophys. Res. Atmos.*, **125 (17)**, e2020JD032 624, doi: 10.1029/2020JD032624.

Saunders, P. M., 1968: Radiance of sea and sky in the infrared window 800-1200 cm−1. J. *Opt. Soc. Am.*, **58 (5)**, 645–652.

Schalles, M. and G. Blumr¨oder, 2012: Calculation of the effective emissivity of blackbodies made of alumina. *Meas. Sci. Technol.*, **23**, doi:10.1088/0957-0233/23/7/074023.

Segelstein, D. J., 1981: The complex refractive index of water. M.S. thesis, Univ. Missouri–Kansas City, 167 pp.

Smith, W. L., et al., 1996: Observations of the infrared properties of the ocean: Implications for the measurement of sea surface temperature via satellite remote sensing. *Bull. Am. Meteorol. Soc.*, **77**, 41–51.

Stegmann, P. G. and P. Yang, 2017: A regional, size-dependent, and causal effective medium model for asian and saharan mineral dust refractive index spectra. *Journal of Aerosol*

Science, **114**, 327–341, doi:10.1016/j.jaerosci.2017.10.003.

Strow, L. L., S. E. Hannon, S. D. Souza-Machado, H. E. Motteler, and D. Tobin, 2003: An overview of the AIRS radiative transfer model. *IEEE Trans. Geosci. Remote Sensing*, **41 (2)**, 303–313.

van Delst, P., N. R. Nalli, J. Jung, Y. Han, Q. Liu, and J. Derber, 2009: Implementation of a new infrared sea surface emissivity model in the Community Radiative Transfer Model (CRTM). *2nd Workshop on Remote Sensing and Modeling of Surface Properties*, Météo France, Toulouse, France.

Watts, P., M. Allen, and T. Nightingale, 1996: Sea surface emission and reflection for radiometric measurements made with the Along-Track Scanning Radiometer. *J. Atmos. Ocean. Tech.*, **13**, 126–141.

Wieliczka, D. M., S. Weng, and M. R. Querry, 1989: Wedge shaped cell for highly absorbent liquids: Infrared optical constants of water. *Appl. Opt.*, **28**, 1714–1719.

Wu, X. and W. L. Smith, 1996: Sensitivity of sea surface temperature retrieval to sea surface emissivity. *ACTA Meteorol. Sinica*, **10**, 376–384, engl. Transl.

Wu, X. and W. L. Smith, 1997: Emissivity of rough sea surface for 8–13μ m: Modeling and validation. *Appl. Opt.*, **36**, 1–11.

EDITOR'S NOTE

It is a pleasure to present the Summer 2021 issue of the JCSDA Quarterly Newsletter. While many of us have enjoyed some well-deserved vacation time during the past couple of months, it is hard to tell from the relentless pace of activity. The JCSDA resumed its Annual Science and Technical Workshop virtually in early June, after foregoing the event in 2020 due to the COVID-19 pandemic, reviewing not one but two years of scientific development.

This issue features a pair of science articles. One, by Byoung-Joo Jung and co-authors, outlines the formulation of static background covariance within the framework of the Joint Effort for Data assimilation Integration for the US Air Force's Model for Prediction Across Scales (MPAS.) This is an exciting early application using elements of JEDI in an operational modeling system. In the other, Nick Nalli and co-authors address the problem of sea-surface properties as boundary conditions for numerical weather prediction systems with an improved infrared sea-surface emissivity model for the Community Radiative Transfer Model (CRTM.) Both of these works were contributed to the JCSDA Symposium during the Annual AMS meeting in January, 2021, and invited for inclusion in the Quarterly to present them to a broader segment of our community than the virtual forum for that meeting was able to provide.

The dynamic nature of the JCDSA's mission is reflected in its workforce. This Summer we have bid farewell to some key contributors, including Dick Dee and Wei Han. But we also have welcomed new colleagues, including Eric Lingerfelt, Francois Herbert, Heli Soell, and Steven Vahl. Each of them has been kind enough to provide a short biographical sketch for this issue, so that you can get to know a little bit about them and the work that they are doing with the JCSDA.

Jim Yoe

Editor

PEOPLE

Eric Lingerfelt

Eric Lingerfelt joined the JCSDA in April 2021 as a Software Engineer working in the JEDI core team. As a contributor to the Research Repository for Data and Diagnostics (R2D2), he supports JEDI users by designing and implementing tools to manipulate, ingest, access, and archive model data and observations in near real-time. In addition, Eric assists the JEDI team with management and maintenance of centralized R2D2 databases on several HPC platforms and the Amazon cloud. He is also involved with development and enhancement of the Experiments and Workflows Orchestration Kit (EWOK) system and Solo software package capabilities.

Originally from a small mountain town in Tennessee between the Appalachian Trail and Dolly Parton's birthplace in the Smoky Mountains, Eric received his undergraduate education at East Tennessee State University in mathematics and physics, where he conducted his senior year research at Kitt Peak National Observatory on the SARA 0.9-meter telescope near Tucson, Arizona. He received his Master of Science degree in physics with a concentration in astrophysics from the University of Tennessee in Knoxville and began his career as an Information Technology Specialist for UT's Department of Physics and Astronomy in 2003. From 2003 to 2009, he worked at Oak Ridge National Laboratory developing the Computational Infrastructure for Nuclear Astrophysics (CINA) SaaS platform, which provides over 100 easy-to-use online tools for stellar explosive studies of novae, x-ray bursts, and supernovae. CINA continues to assist the astrophysics community to this day, with registered users from over 40 countries and almost 200 institutions.

In 2009, he accepted a position as a Technical Staff Member and Software Engineer at ORNL, where he led the design and implementation of several award-winning computational infrastructures in the areas of nuclear astrophysics, nanoscale materials science, Big Bang cosmology, supernovae modeling, environmental science, and isotope sales and distribution. These n-tier systems provided end-users with highly interactive, intuitive user interfaces enabling scientific data analysis, management, modeling, collaboration, and visualization in combination with secure web services, cloud resources, petabyte-scale storage, and several HPC platforms including Jaguar and Titan at the OLCF and Edison, Hopper, and Cori at NERSC.

In 2017, Eric joined UCAR as EarthCube Technical Officer and Senior Software Engineer, where he led the design of technical architectures for the NSF EarthCube program and the implementation of the GeoCODES cyberinfrastructure platform enabling Earth science data providers and consumers to register, search, discover, and access resources from dozens of NSF data repositories using modern web standard methods and technologies. It was during this time that he founded Pandia Software (https://pandiasoftware.com) to continue his work developing and enhancing software platforms for US Department of Energy astrophysics initiatives.

Eric currently resides in Fort Collins, Colorado with his partner Rowena. He enjoys playing bass guitar in the band "Jeebus Heathens," disc golf, hiking, biking, fishing, archery, and tubing the Poudre River. He also enjoys the local breweries and distilleries and listening to music on vinyl records.

François Herbert

François Hebert joined the JCSDA in August 2021 as a Project Scientist on the JEDI model interfaces team and liaison to the NOAA EMC. His initial work will improve the modeling of satellite observation operators to help prepare JEDI for operational work at NOAA.

François is a computational physicist from a background in astronomy. He has studied sedimentation in the interior of white dwarf stars, explored shock-capturing algorithms for simulations of neutron stars and accretion discs around black holes, and used ray tracing to make visually accurate simulations of what two colliding black holes would look like to an (unfortunate?) nearby astronaut. He previously tested the waters of atmospheric science as an NCAR intern, and he's thrilled to be returning to the field with the JCSDA.

François has rotated through hobbies ranging from classical piano to competitive ballroom dance. Most recently, he spends his free time cycling uphill in search of views of mountain layers fading into the hazy distance.

Heli Soell

Heli Soell joined UCAR in June of 2021 as an Administrator assisting with the business operations of the JCSDA. Her main duties include support in the areas of HR & general Administration, Procurement, Budgeting and Proposals.

A Boulder native, Heli received her BFA from NYU's Tisch School of the Arts for Dance and Musical Theater. After knee injuries sidelined a career as a performer, she transitioned into the production world of film and television in Los Angeles, most notably as the Production Coordinator on NBC's "The Voice" for seasons 1-5. Prior to leaving "The Voice" for a return to New York and live theater production, Heli danced for Kelly Clarkson's premiere performance of her hit holiday song "Underneath the Tree". Back in New York, she continued to develop her administrative, project management and financial skills working for a number of internationally recognized arts venues and institutions including BAM (Brooklyn Academy of Music), The Shed and the Brooklyn Museum.

While the 2020 pandemic brought Heli back to her hometown of Boulder, she's thrilled that she landed at UCAR and is excited to bring her unique perspective and love of coordination and numbers to the JCSDA team. In her spare time, Heli is an avid reader, yogi and bottomless pit of true crime documentaries and podcasts.

Steven Vahl

Steven Vahl joined the JCSDA in Boulder in March 2021 as a Software Engineer on the JEDI core team. He is the team liaison to the United Kingdom Meteorological Office (Met Office or UKMO), working on the integration of the Met Office models with JEDI. Prior to that he worked at the National Center for Atmospheric Research (NCAR) for over two years, integrating the MPAS model with JEDI.

Steve has over 25 years of experience as a software engineer, mostly in the private sector. He worked for over 12 years developing software for portable near-infrared (NIR) spectrometers, including projects to identify minerals and pharmaceuticals by their NIR spectral signature. He has also worked in biotech and business management software.

Steve received his Bachelor's degree in Mathematics from Washington University in St. Louis, and Master's degree in Mathematics from the University of Illinois at Urbana-Champaign. He is originally from Omaha, Nebraska and has now lived in Colorado for over 25 years.

Apart from work, Steve enjoys watching and discussing Marvel and Star Wars movies and shows with his two teenage sons. You will also frequently find him on a pickleball court.

SCIENCE CALENDAR

Meetings of Interest

TITLE	DATE	LOCATION	WEBSITE
CRTM User and Developer Workshop	TBD	Virtual	
International Precipitation Working Group	October 18-22, 2021	Virtual	https://www.isac.cnr.it/~ipwg/
10th AMS Symposium on the JCSDA	January 23-27, 2022	Houston, TX	https://annual.ametsoc.org/index.cfm/2022/program-events/conferences-and-symposia/10th-ams-symposium-on-the-joint-center-for-satellite-data-assimilation-jcsda/
AMS JEDI Short Course	January TBD	TBD	
JCSDA Annual Executive Team Retreat	February 2022 TBD	TBD	
International Symposium on Data Assimilation	June 6-10, 2022	Fort Collins, CO	https://www.cira.colostate.edu/conferences/isda/
19th JCSDA Technical Review Meeting and Science Workshop	June 1, 2022, TBD	TBD	

CAREER OPPORTUNITIES

Opportunities in support of JCSDA may be found at https://www.jcsda.org/opportunities as they become available.